Supporting information for
Best practice of materials modeling in electrocatalysis exemplified by oxygen evolution reaction on pentlandites

Maksim Sokolov[1,2], Katharina Doblhoff-Dier[3,*], Kai S. Exner[1,2,4,*]

[1] *University Duisburg-Essen, Faculty of Chemistry, Theoretical Inorganic Chemistry, Universitätsstraße 5, 45141 Essen, Germany*

[2] *Cluster of Excellence RESOLV, 44801 Bochum, Germany*

[3] *Leiden Institute of Chemistry, Leiden University, P.O. Box 9502, Leiden 2300 RA, The Netherlands*

[4] *Center for Nanointegration (CENIDE) Duisburg-Essen, 47057 Duisburg, Germany*

* Corresponding author: kai.exner@uni-due.de; k.doblhoff-dier@lic.leidenuniv.nl
ORCID: 0000-0003-2934-6075 (KSE)

S1 Extended computational details

In this section, we provide complete details on the computational parameters and utilized methods.

Table S1. Complete list of computational parameters used for all calculations.

Bulk lattice constant	9.52 Å
Slab geometry	$a = b = 13.46$ Å, $c = 26.48$ Å, 16 Å vacuum gap, $\alpha = \beta = 90°$, $\gamma = 120°$, 10 metal layers thick, 136 atoms
Software	VASP 6.3.0[1]
Exchange-correlation functional	RPBE[2]
Pseudopotentials	Ultrasoft potentials[3] using projector augmented wave (PAW)[4] method
Fe valence configuration	$3d^7 4s^1$, valence 8, energy cutoff 268 eV, generated 06.09.2000
Ni valence configuration	unspecified configuration, valence 10, energy cutoff 270 eV, generated 06.09.2000
S valence configuration	$3s^2 3p^4$, valence 6, energy cutoff 400 eV, generated 17.01.2003
O valence configuration	$2s^2 2p^4$, valence 6, energy cutoff 400 eV, generated 08.04.2002
H valence configuration	$1s^1$, valence 1, energy cutoff 250 eV, generated 15.06.2001
Spin polarization	Non-spin polarized calculations

Plane wave cut-off	500 eV
Smearing	Gaussian smearing
Dispersion correction	Grimme DFT-D3 correction[5]
Self-consistent field convergence criteria	Energy difference between iterations is less than 10^{-4} eV
Geometry convergence criteria	Forces are smaller than 0.05 eV $Å^{-1}$
k-points	$6 \times 6 \times 1$
k-points, ZPE calculation	Γ-point only

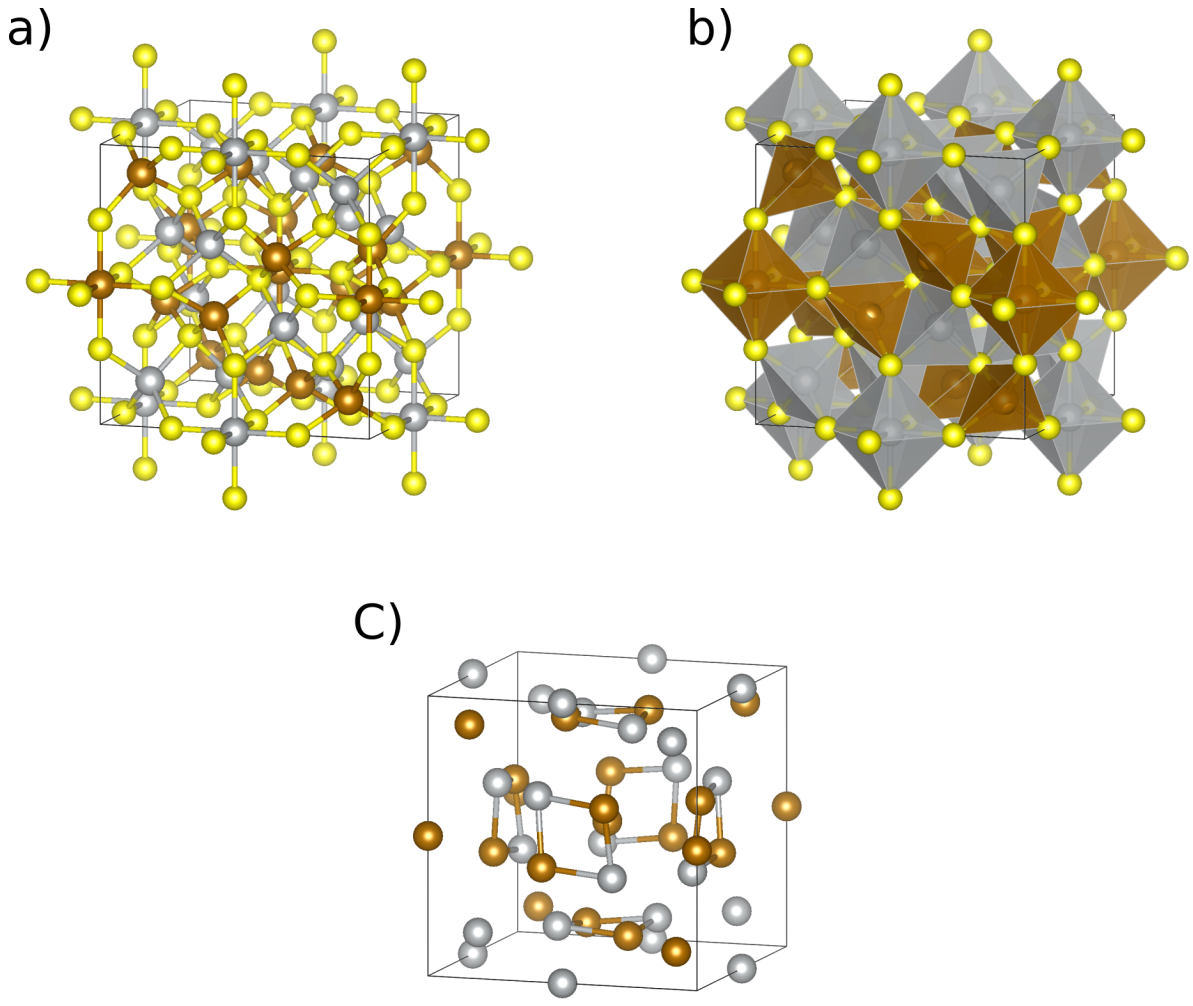

Figure S1. Bulk structure of the most energetically favorable $Fe_{4.5}Ni_{4.5}S_8$ pentlandite. a) complete unit cell; b) complete unit cell with polyhedrons; c) unit cell where sulfur atoms are hidden.

In equations 1-4 of the main text, we introduce the free energy changes ΔG_j^0 $(j = 1, 2, 3, 4)$ of the elementary steps of oxygen evolution (OER). The numerical values for these free energy differences are calculated from the equation $\Delta G_j^0 = \Delta E_{\mathrm{DFT}} + \Delta\mathrm{ZPE} - T\Delta S$, where[6]:

- ΔE_{DFT} is the difference of the DFT-computed energies between the final and initial states.
- ΔZPE is the zero-point energy contribution in the harmonic oscillator approximation, which is calculated from the real parts of vibrational frequencies of the final and initial states: $\mathrm{ZPE} = \frac{1}{2}\sum_{i=1}^{3n-6} h\nu_i$ where n is the number of atoms that are allowed to vibrate in the calculation, h is the Planck's constant, and ν is the frequency of the vibration that is acquired from the phonon calculations using a finite-difference approach in VASP.
- Temperature, $T = 298.15$ K, and the entropy S consists of the standard entropy of gaseous water and gaseous hydrogen, obtained from thermodynamic tables and converted to the respective reference conditions (*vide infra*), and the vibrational entropy of the intermediate structures evaluated by the equation $TS = k_{\mathrm{B}}T\sum_{i=1}^{3n-6}\left(\frac{x_i}{(e^{x_i}-1)} - \ln(1-e^{-x_i})\right)$, where $x_i = \frac{h\nu_i}{k_{\mathrm{B}}T}$.
- Note that the application of the computational hydrogen electrode (CHE) approach requires the use of gaseous water at T = 298.15 K and p = 0.035 bar and gaseous hydrogen at T = 298.15 K, p = 0.035 bar, and U = 0 V vs. standard hydrogen electrode (SHE), pH = 0 as the reference states in the analysis of the ΔG_j^0 values.

To avoid the occurrence of gas-phase errors in the calculation of the O_2 molecule by plane-wave DFT, we make use of the concept of gas-phase error corrections in that the standard free energy of the overall water oxidation is related to the experimental value of 4.92 eV = $4eU^0_{\mathrm{OER}}$.[7]

S2 Catalytic activity descriptors

For a definition of the activity descriptors thermodynamic overpotential, η_{TD}[6], and $G_{\max}(U)$[8], we recall the mononuclear mechanism of the OER from the main text:

* + H_2O	$\rightarrow$ *OH + H^+ + e^-	$\Delta G_1 = \Delta G_1^0 - eU$	**(1)**
*OH	$\rightarrow$ *O + H^+ + e^-	$\Delta G_2 = \Delta G_2^0 - eU$	**(2)**
*O + H_2O	$\rightarrow$ *OOH + H^+ + e^-	$\Delta G_3 = \Delta G_3^0 - eU$	**(3)**
*OOH	$\rightarrow$ * + $O_{2(g)}$ + H^+ + e^-	$\Delta G_4 = 4.92 - \Sigma_{i=1}^{3}\Delta G_i - 4eU$	**(4)**

η_{TD} is defined as:

$$\eta_{\mathrm{TD}} = \max(\Delta G_j^0 - 1.23)\,/e \qquad \textbf{(5)}$$

where e is the elementary charge. Note that the descriptor η_{TD} is given in the unit [V].

To define $G_{\max}(U)$, we introduce the expressions for the adsorption free energies of the reaction intermediates *OH, *O, and *OOH:

$$G_{*} = 0 \quad (6)$$

$$G_{*\mathrm{OH}} = \Delta G_1 = \Delta G_1^0 - eU \quad (7)$$

$$G_{*\mathrm{O}} = \Delta G_1 + \Delta G_2 = \Delta G_1^0 + \Delta G_2^0 - 2eU \quad (8)$$

$$G_{*\mathrm{OOH}} = \Delta G_1 + \Delta G_2 + \Delta G_3 = \Delta G_1^0 + \Delta G_2^0 + \Delta G_3^0 - 3eU \quad (9)$$

$$G_{*+\mathrm{O}_2(g)} = \Sigma_{i=1}^{4} \Delta G_i = 4.92 - 4eU \quad (10)$$

The descriptor $G_{\max}(U)$ refers to the largest free energy span between all intermediate states of equations 6-10 in the free energy diagram (FED) at a given potential U:

$$\begin{aligned} G_{\max}(U) = \max\{ & G_{*\mathrm{OH}}(U) - G_{*}(U);\ G_{*\mathrm{O}}(U) - G_{*}(U);\ G_{*\mathrm{OOH}}(U) - G_{*}(U); \\ & G_{*\mathrm{O}}(U) - G_{*\mathrm{OH}}(U);\ G_{*\mathrm{OOH}}(U) - G_{*\mathrm{O}}(U);\ G_{*+\mathrm{O}_2(g)}(U) - G_{*\mathrm{OOH}}(U); \\ & G_{*\mathrm{OOH}}(U) - G_{*\mathrm{OH}}(U);\ G_{*+\mathrm{O}_2(g)}(U) - G_{*\mathrm{O}}(U); \\ & G_{*+\mathrm{O}_2(g)}(U) - G_{*\mathrm{OH}}(U)\} \end{aligned} \quad (11)$$

Alternatively, one could also express $G_{\max}(U)$ in terms of ΔG_j:

$$G_{\max}(U) = \max\left\{ \sum_{i=m}^{i=l} \Delta G_i \right\} \quad (12)$$

where $m,\ l$ are integer iterators that obey $1 \leq m \leq l < 4$.

The descriptor $G_{\max}(U)$ is related to the current density, *j*, by the equation[8,9]:

$$j(U) = \frac{4k_B T}{h} e\Gamma_{\mathrm{act}} \exp\left[\frac{-(G_{\max}(U) + \beta)}{k_B T}\right] \quad (13)$$

In equation (13), β is the Brønsted–Evans–Polanyi (BEP) intercept constant, which we assume to be 0.4 eV based on a benchmarking of experimental transition state free energies with DFT-based $G_{\max}(U)$ values.[8] Γ_{act} is the density of active sites, which amounts to $6.4 \times 10^{13}\mathrm{cm}^{-2}$ for a single active site in the 2×1 cell; *T* is the temperature in Kelvin, and k_B, *h,* and *e* are the Boltzmann constant, Planck constant, and the elementary charge, respectively.

S3 Single reaction intermediate on the surface

In this section, we compile all the data in terms of adsorption energies for a single *OH, *O, and *OOH reaction intermediate on the Pn(111) surface. By comparing the adsorption energies at $U = 1.53$ V vs RHE for the most stable configurations of each intermediate, it is evident that the *O adsorbate is energetically preferred. This enables us to construct the Pourbaix diagram based on oxygenated surfaces (cf. section 3.1 in the main text).

Tables S2-S4 indicate further interesting facts on the conducted DFT calculations for the considered adsorbates on the Pn(111) surface. The notation "strict" is used when an adsorbate is placed directly atop sulfur, while in other cases adsorbates are considered to be between two metal atoms. First, the relaxation from a different initial guess could lead to the same final configuration,

but the energies of these configurations can be very different. As an example, if we consider the *O adsorbate in its initial configuration "$S_{oct}(Ni_{oct}\text{-}2Fe_{tet})$ (strict)" (S3-14 in Table S3), we observe that this structure converges to *O between "$Fe_{tet1}\text{-}Fe_{tet2}$" (adsorption energy of –3.41 eV). When using "Fe_{tet2}" (S3-2 in Table S3) as the initial configuration, it turns out that the *O adsorbate also converges to *O between "$Fe_{tet1}\text{-}Fe_{tet2}$"; however, in this case the adsorption energy amounts to –1.93 eV. The difference in adsorption energy for *O in the same site goes hand in hand with strong structural changes in the surface as summarized in Table S5. The difference of 1.48 eV in the final configurations can thus only be attributed to the fact that the path of relaxation of the underlying surface has a strong impact on the final energy. Moreover, if we start with the configuration "*O between $Fe_{tet1}\text{-}Fe_{tet2}$", this configuration converges to "Fe_{hollow}" with a significantly higher energy than one would get if the initial guess was "Fe_{hollow}". Second, the *O reaction intermediate interacts noticeably with the sulfur atoms on the surface, which complicates the process of finding the most stable coverage.

Finally, we observe that the *OOH intermediate frequently disassociates into *OH and *O. This finding, in turn, facilitates the modeling of the OER mononuclear mechanism as this pathway can only proceed on sites where *OOH is stable.

Table S2. Adsorption energies of a single *OH adsorbate on the Pn(111) surface. The energetically most favorable configuration is highlighted in bold.

Index	Initial adsorption site	*OH adsorption energy	Adsorption energy at 1.53V	comment/converged configuration
S2-1	Fe_{tet1}	-0.85	-2.38	-
S2-2	Fe_{tet2}	-0.63	-2.16	-
S2-3	Ni_{tet1}	0.90	-0.63	-
S2-4	Ni_{tet2}	0.44	-1.09	-
S2-5	$S_{tet}(2Fe_{tet}\text{-}Ni_{tet})$ / between Fe_{tet2}	0.10	-1.43	-
S2-6	$S_{tet}(Fe_{tet}\text{-}2Ni_{tet})$ / between Ni_{tet2} - Fe_{tet1}	-0.19	-1.72	-
S2-7	$S_{oct}(Ni_{oct}\text{-}2Ni_{tet})$ / between Ni_{tet2}	0.76	-0.77	-
S2-8	Fe_{oct}	0.66	-0.87	converged to $S_{oct}(Fe_{oct}\text{-}2Fe_{tet})$
S2-9	Ni_{oct}	1.47	-0.06	*OH dissociation from the surface
S2-10	Fe_{hollow}	-0.88	-2.41	-
S2-11	Ni_{hollow}	0.78	-0.75	-
S2-12	$S_{oct}(Ni_{oct}\text{-}2Fe_{tet})$ / between $Fe_{tet1}\text{-}Fe_{tet2}$	0.41	-1.12	-
S2-13	$S_{tet}(Fe_{tet}\text{-}2Ni_{tet})$ / between Ni_{tet2}	0.22	-1.31	-
S2-14	**$S_{oct}(Ni_{oct}\text{-}2Fe_{tet})$ (strict)**	**-1.67**	**-3.20**	**converged to *OH between $Fe_{tet1}\text{-}Fe_{tet2}$**
S2-15	$S_{tet}(2Fe_{tet}\text{-}Ni_{te})$ (strict)	0.47	-1.06	converged to *OH between $Fe_{tet2}\text{-}Fe_{tet2}$
S2-16	$S_{tet}(Fe_{tet}\text{-}2Ni_{tet})$ (strict)	-1.29	-2.82	converged to Fe_{tet1}
S2-17	$S_{oct}(Ni_{oct}\text{-}2Ni_{tet})$ (strict)	0.55	-0.98	OH dissociation from the surface
S2-18	$S_{oct}(Fe_{oct}\text{-}2Ni_{tet})$ (strict)	0.11	-1.42	converged to Ni_{tet2}
S2-19	$S_{oct}(Fe_{oct}\text{-}2Fe_{tet})$ (strict)	0.42	-1.11	converged to *OH between $Fe_{tet2}\text{-}Fe_{tet2}$
S2-20	$S_{oct}(Fe_{oct}\text{-}2Ni_{tet})$ / between $Ni_{tet1}\text{-}Ni_{tet2}$	-0.08	-1.61	converged to Ni_{tet2}

S2-21	$S_{oct}(Fe_{oct}\text{-}2Fe_{tet})$ / between Fe_{tet2}	-0.88	-2.41	converged to Fe_{hollow}

Table S3. Adsorption energies of a single *O adsorbate on the Pn(111) surface. The energetically most favorable configuration is highlighted in bold.

Index	Initial adsorption site	*O adsorption energy	Adsorption energy at 1.53V	comment/converged configuration
S3-1	Fe_{tet1}	0.00	-3.06	-
S3-2	Fe_{tet2}	1.13	-1.93	converged to *O between Fe_{tet1}-Fe_{tet2}
S3-3	Ni_{tet1}	1.93	-1.13	converged to *O between Ni_{tet1}-$S_{tet}(2Fe_{tet}\text{-}Ni_{tet})$
S3-4	Ni_{tet2}	1.02	-2.04	converged to *O between Ni_{tet2}-Fe_{tet1}
S3-5	$S_{tet}(2Fe_{tet}\text{-}Ni_{tet})$ / between Fe_{tet2}	2.29	-0.77	converged to *O between Fe_{tet2}-$S_{tet}(2Fe_{tet}\text{-}Ni_{tet})$
S3-6	$S_{tet}(Fe_{tet}\text{-}2Ni_{tet})$ / between Ni_{tet2} - Fe_{tet1}	1.19	-1.87	-
S3-7	$S_{oct}(Ni_{oct}\text{-}2Ni_{tet})$ / between Ni_{tet2}	1.09	-1.97	converged to *O atop $S_{oct}(Ni_{oct}\text{-}2Ni_{tet})$
S3-8	Fe_{oct}	1.75	-1.31	converged to *O atop $S_{oct}(Fe_{oct}\text{-}2Ni_{tet})$
S3-9	Ni_{oct}	1.80	-1.26	converged to *O atop $S_{oct}(Ni_{oct}\text{-}2Ni_{tet})$
S3-10	Fe_{hollow}	-0.19	-3.25	-
S3-11	Ni_{hollow}	2.05	-1.01	-
S3-12	$S_{oct}(Ni_{oct}\text{-}2Fe_{tet})$ / between Fe_{tet1}-Fe_{tet2}	1.65	-1.41	converged to Fe_{hollow}
S3-13	$S_{tet}(Fe_{tet}\text{-}2Ni_{tet})$ / between Ni_{tet2}	1.60	-1.46	-
S3-14	**$S_{oct}(Ni_{oct}\text{-}2Fe_{tet})$ (strict)**	**-0.35**	**-3.41**	**converged to *O between Fe_{tet1}-Fe_{tet2}**
S3-15	$S_{tet}(2Fe_{tet}\text{-}Ni_{te})$ (strict)	1.80	-1.26	converged to *O between Fe_{tet2}-Fe_{tet2}
S3-16	$S_{tet}(Fe_{tet}\text{-}2Ni_{tet})$ (strict)	0.94	-2.12	converged to *O between Fe_{tet1}-$S_{tet}(Fe_{tet}\text{-}2Ni_{tet})$
S3-17	$S_{oct}(Ni_{oct}\text{-}2Ni_{tet})$ (strict)	1.09	-1.97	-
S3-18	$S_{oct}(Fe_{oct}\text{-}2Ni_{tet})$ (strict)	1.38	-1.68	converged to *O between Ni_{tet1}-$S_{oct}(Fe_{oct}\text{-}2Ni_{tet})$
S3-19	$S_{oct}(Fe_{oct}\text{-}2Fe_{tet})$ (strict)	1.21	-1.85	converged to *O between Fe_{tet2}-Fe_{tet2}
S3-20	$S_{oct}(Fe_{oct}\text{-}2Ni_{tet})$ / between Ni_{tet1}-Ni_{tet2}	1.29	-1.77	converged to Ni_{hollow}
S3-21	$S_{oct}(Fe_{oct}\text{-}2Fe_{tet})$ / between Fe_{tet2}	1.65	-1.41	converged to Ni_{hollow}

Table S4. Adsorption energies of a single *OOH adsorbate on the Pn(111) surface. The energetically most favorable configuration is highlighted in bold.

Index	Initial adsorption site	*OOH adsorption energy	Adsorption energy at 1.53V	comment/converged configuration
S4-1	Fe_{tet1}	2.25	-2.34	-
S4-2	Fe_{tet2}	2.35	-2.24	-
S4-3	Ni_{tet1}	3.52	-1.07	-
S4-4	Ni_{tet2}	3.40	-1.19	-
S4-5	$S_{tet}(2Fe_{tet}\text{-}Ni_{tet})$ / between Fe_{tet2}	2.37	-2.22	converged to Fe_{tet2}
S4-6	$S_{tet}(Fe_{tet}\text{-}2Ni_{tet})$ / between Ni_{tet2} - Fe_{tet1}	1.51	-3.08	converged to Fe_{tet1}
S4-7	$S_{oct}(Ni_{oct}\text{-}2Ni_{tet})$ / between Ni_{tet2}	4.11	-0.48	*OH dissociates from the surface, *O is on $S_{oct}(Ni_{oct}\text{-}2Ni_{tet})$

S4-8	Fe_{oct}	1.52	-3.07	*OH is on Ni_{tet2}, *O is between Fe_{tet2}-$S_{oct}(Fe_{oct}$-$2Fe_{tet})$
S4-9	Ni_{oct}	4.15	-0.44	*OOH dissociates from the surface
S4-10	Fe_{hollow}	1.80	-2.79	*OH is on Fe_{tet1}, *O is on Fe_{hollow}
S4-11	Ni_{hollow}	4.12	-0.47	-
S4-12	$S_{oct}(Ni_{oct}$-$2Fe_{tet})$ / between Fe_{tet1}-Fe_{tet2}	1.33	-3.26	*OH is on Fe_{tet1}, *O is on Fe_{hollow}
S4-13	$S_{tet}(Fe_{tet}$-$2Ni_{tet})$ / between Ni_{tet2}	3.39	-1.20	converged to Ni_{tet2}
S4-14	$S_{oct}(Ni_{oct}$-$2Fe_{tet})$ (strict)	1.38	-3.21	*OH is in Fe_{hollow}, *O is on $S_{oct}(Ni_{oct}$-$2Fe_{tet})$
S4-15	$S_{tet}(2Fe_{tet}$-$Ni_{te})$ (strict)	1.83	-2.76	*OH is on Ni_{tet1}, *O is between Fe_{tet2}
S4-16	**$S_{tet}(Fe_{tet}$-$2Ni_{tet})$ (strict)**	**1.35**	**-3.24**	**converged to Fe_{tet1}**
S4-17	$S_{oct}(Ni_{oct}$-$2Ni_{tet})$ (strict)	4.14	-0.45	*OH dissociates from the surface, *O is on $S_{oct}(Ni_{oct}$-$2Ni_{tet})$
S4-18	$S_{oct}(Fe_{oct}$-$2Ni_{tet})$ (strict)	-	-	not converged, OH dissociates from the surface
S4-19	$S_{oct}(Fe_{oct}$-$2Fe_{tet})$ (strict)	0.62	-3.97	*OH is between Fe_{tet1}-$Fe_{tet2,}$ *O is on $S_{oct}(Fe_{oct}$-$2Fe_{tet})$
S4-20	$S_{oct}(Fe_{oct}$-$2Ni_{tet})$ / between Ni_{tet1}-Ni_{tet2}	3.19	-1.40	converged to Ni_{tet2}
S4-21	$S_{oct}(Fe_{oct}$-$2Fe_{tet})$ / between Fe_{tet2}	0.75	-3.84	*OH is between Fe_{tet2}-Fe_{tet2}, *O is on $Fe_{hollow,}$

To explain the differences in energies of similar converged structures, we measured the root sum squared (RSS) of displacement of all slab atoms with respect to the pristine slab. The results are compiled in **Table S5.** In almost all cases, a larger RSS corresponds to a lower energy. A clear exception is the couple S3-12 and S3-10 (*O in Fe_{hollow}). We conclude that the potential energy surface of Pn is complex, and a thorough sampling of different geometries is required to avoid getting stuck in a local minimum when optimizing adsorbate configurations.

Table S5. Structural changes of the slab for structures that converged to the same configuration from different initial guesses. Structural changes are measured with respect to the pristine slab. Indexes correspond to the ones from Tables S2-S4.

Index	Adsorption energy, eV	Root sum squared of displacements
S2-12	0.41	1.44
S2-14	-1.67	2.13
S2-16	-1.29	1.52
S2-1	-0.85	1.16
S2-18	0.11	1.57
S2-20	-0.08	1.63
S2-4	0.44	1.41
S2-15	0.47	1.06
S2-19	0.42	1.41
S2-21	-0.88	0.70
S2-10	-0.88	0.63
S3-2	1.13	1.59
S3-14	-0.35	2.35

S3-9	1.80	0.48
S3-7	1.09	1.18
S3-12	1.65	1.46
S3-10	-0.19	0.35
S3-11	2.05	0.56
S3-20	1.29	1.76
S3-21	1.65	1.31
S4-1	2.25	1.21
S4-6	1.51	1.61
S4-16	1.35	1.89
S4-2	-2.24	1.47
S4-5	-2.22	0.95
S4-4	3.40	1.43
S4-13	3.39	1.63
S4-20	3.19	1.72
S4-12	1.33	1.64
S4-10	1.80	0.56

Process of building the stability and Pourbaix diagrams

We justify our choice of a particular 4*O configuration due to the following considerations: as we discussed in section S3, convergence pathways of Pn are hard to predict. One aspect we noticed is that the use of *O adsorbates on sulfur atoms leads to energetically preferable configurations. This gave us the idea to perform a calculation where all tetrahedral sulfur sites are occupied with *O (cf. **Figure S2**). To have a reference point, we also placed 4*O in the hollow sites, which, based on the data of **Table S3**, is also a potential candidate for the 4*O surface. We obtain that the former relaxed configuration is by 1.1 eV energetically preferred over the latter, and this finding corroborates our starting point for the construction of the stability and Pourbaix diagrams.

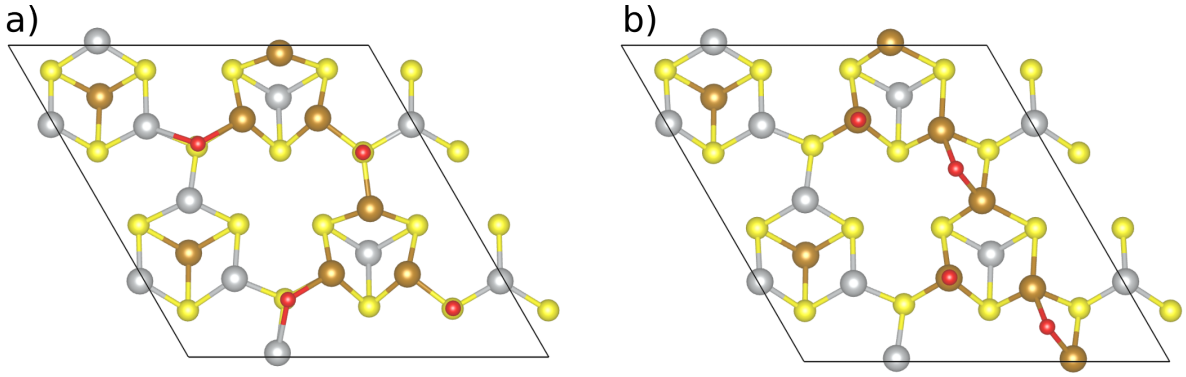

Figure S2. Selected configuration used as a starting point for the iterative procedure described in **Figure 2** of the main text. a) Initial guess, b) relaxed configuration.

The necessity of the iterative procedure described in the main text is best demonstrated by the case of the 12*O surface (100% coverage when counting the metal sites of the 2×1 superslab). In **Figure S3**, we show two different 12*O surfaces, namely one resulting from a chemically intuitive naive guess that is agnostic of the data from **Tables S2-S4** by placing all *O atoms directly atop metal sites, and the other one is related to the introduced iterative procedure. These configurations differ significantly in terms of oxygen positioning, and the energy difference amounts to 2.76 eV in favor of the iterative procedure.

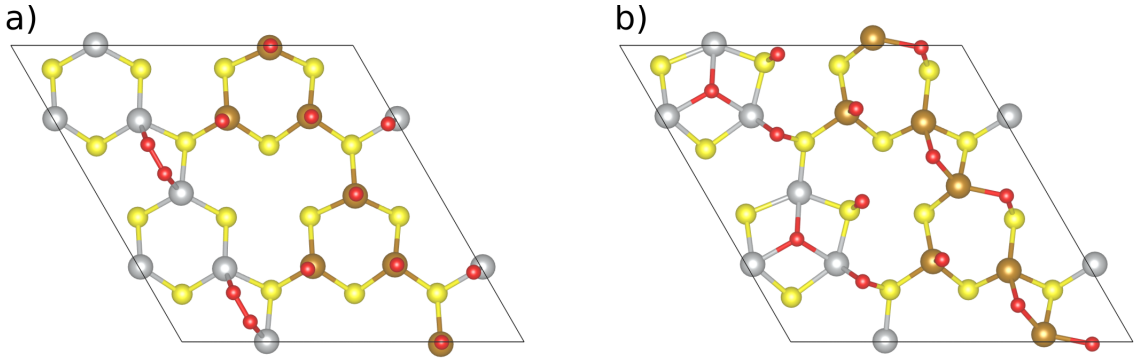

Figure S3. Relaxed structures for a) naive guess of the 12*O coverage; b) 12*O coverage based on the introduced iterative procedure.

S4 Reconstruction of the 24*O surface

Figure S4 illustrates that with a sufficiently large oxygen coverage, sulfur begins to desorb from the surface in the form of SO_2. This process has been reported in previous experimental works. As such, we decided to avoid mixing of these two different phenomena (OER and surface reconstruction) in our modeling as there is no clear way of decoupling them at a later stage.

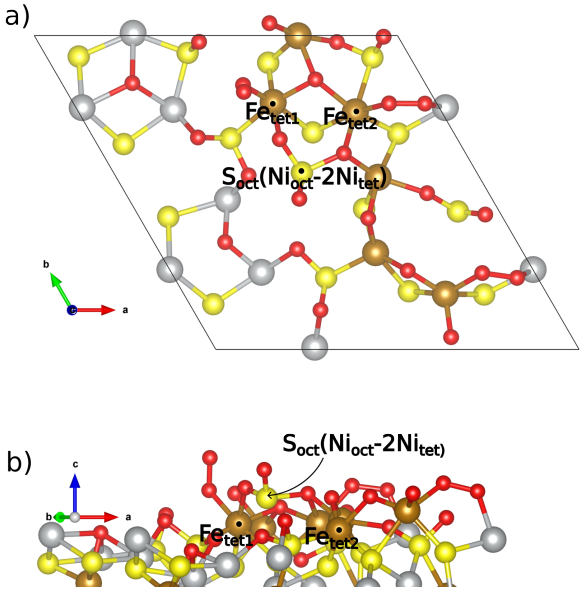

Figure S4. Demonstration of sulfur desorption from the 24*O surface in the form of SO_2.

S5 Modeling of the OER

In this section, we summarize the data of the descriptor $G_{\max}(1.53\mathrm{V})$ (cf. **Table S5**) and visualize the simulated OER pathways (cf. **Table S6**). Free energy diagrams for the cases a) – f) are provided in **Figure 4** of the main text, whereas the cases g) – i) are discussed in **Figure 5** of the main text.

In the main text, we present the results for the 1×1 cell that is obtained by halving the corresponding 2×1 cells and reoptimizing the geometry. However, we also utilized a different approach, in which we halved the 20*O structure and created the *OH, *OOH and * initial guesses by manual input. The latter approach results in an even larger discrepancy of $G_{\max}(1.53\mathrm{V})$ between the 1×1 ($G_{\max}(1.53\mathrm{V}) = 1.06$ eV) and 2×1 ($G_{\max}(1.53\mathrm{V}) = 0.33$ eV) cells for the Fe_{tet1} adsorption site, thus providing further evidence that the initial guess play a major role to obtain reliable energetics.

Table S6. Summary of $G_{\max}(1.53\ \mathrm{V})$ for various Pn surfaces, sites, and solvation treatments.

Index	System description	$G_{\max}(1.53\mathrm{V})$, eV	Limiting free energy span
a)	Pristine surf., Fe_{tet1} ads. site	1.75	*O→$O_2(g)$
b)	Pristine surf., Ni_{tet1} ads. site	1.14	*O→*OOH
c)	20*O surf., Fe_{tet1} ads. site	0.33	*O→*OOH
d)	20*O surf., Ni_{tet1} ads. site	0.95	*O→*OOH
e)	10*O surf. (halved slab), Fe_{tet1} ads. site	0.53/1.06	*O→*OOH
f)	10*O surf. (halved slab), Ni_{tet1} ads. site	1.00	*O→*OOH
g)	20*O surf., Fe_{tet1} ads. site, single water molecule	0.78	*OH→*O
h)	20*O surf., Fe_{tet1} ads. site, two water molecules	0.32	*O→*OOH
i)	20*O surf., Fe_{tet1} ads. site, VASPsol	0.24	*O→*OOH

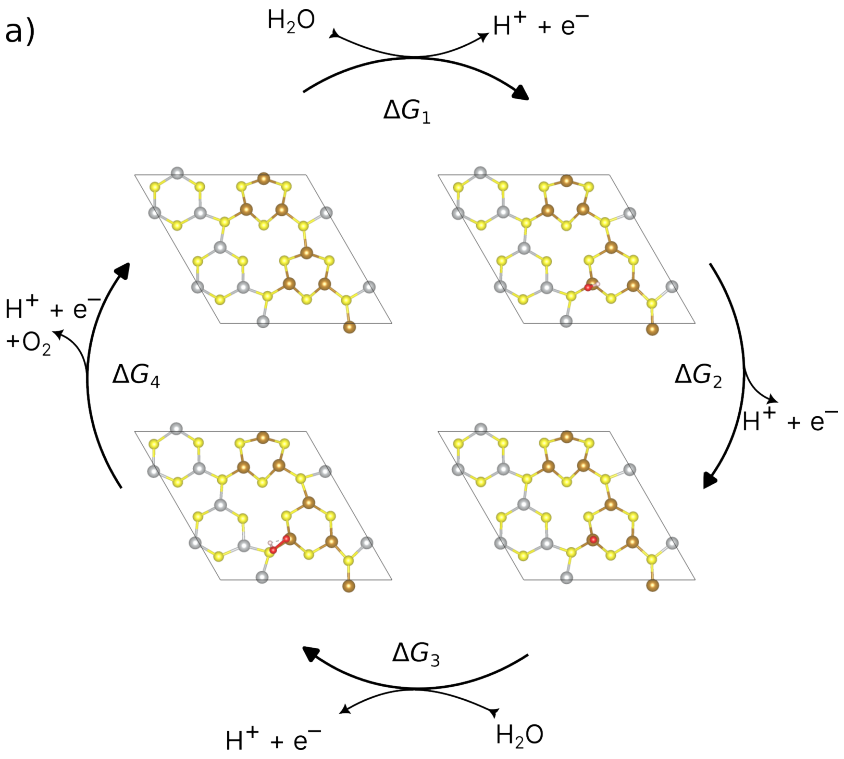
a)
H2O
H+ + e−
ΔG1
H+ + e−
+O2
ΔG4
ΔG2
H+ + e−
ΔG3
H+ + e−
H2O

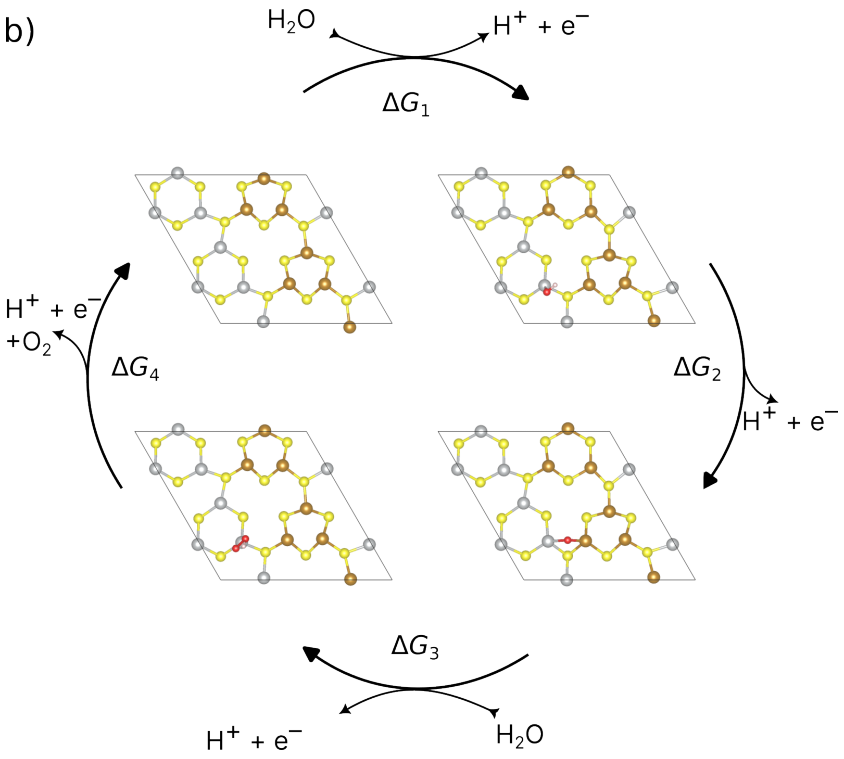
b)
H2O
H+ + e−
ΔG1
H+ + e−
+O2
ΔG4
ΔG2
H+ + e−
ΔG3
H+ + e−
H2O

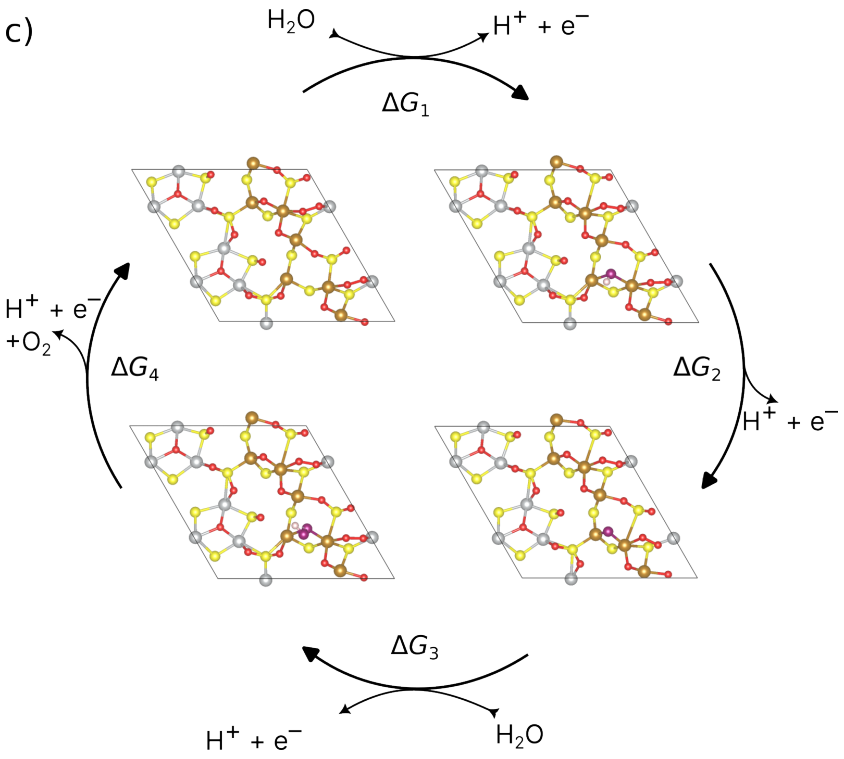
c)
H2O
H+ + e−
ΔG1
H+ + e−
+O2
ΔG4
ΔG2
H+ + e−
ΔG3
H+ + e−
H2O

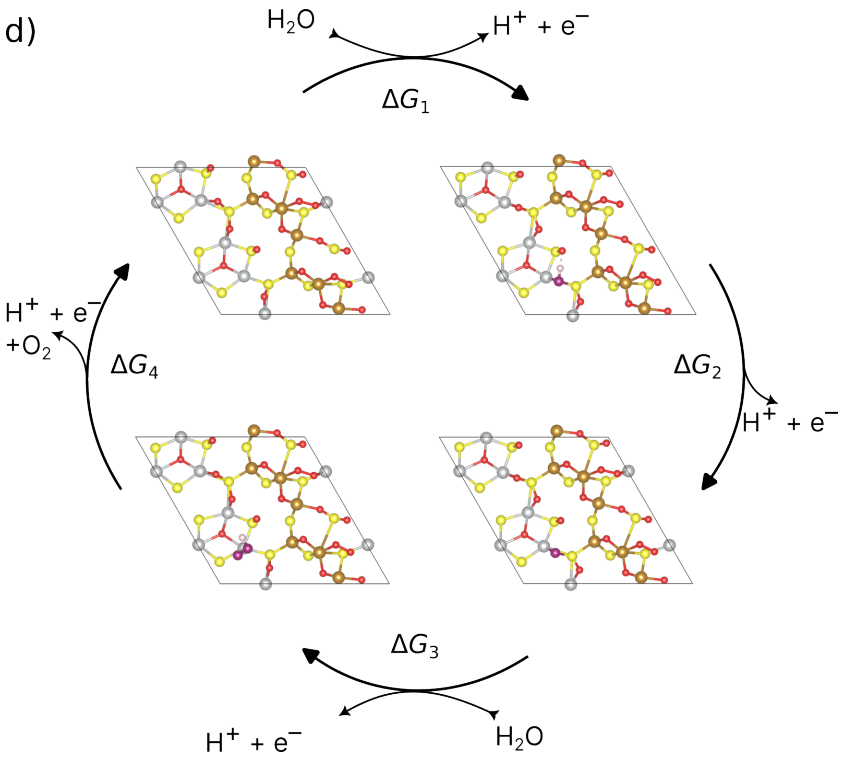
d)
H2O
H+ + e−
ΔG1
H+ + e−
+O2
ΔG4
ΔG2
H+ + e−
ΔG3
H+ + e−
H2O

e)

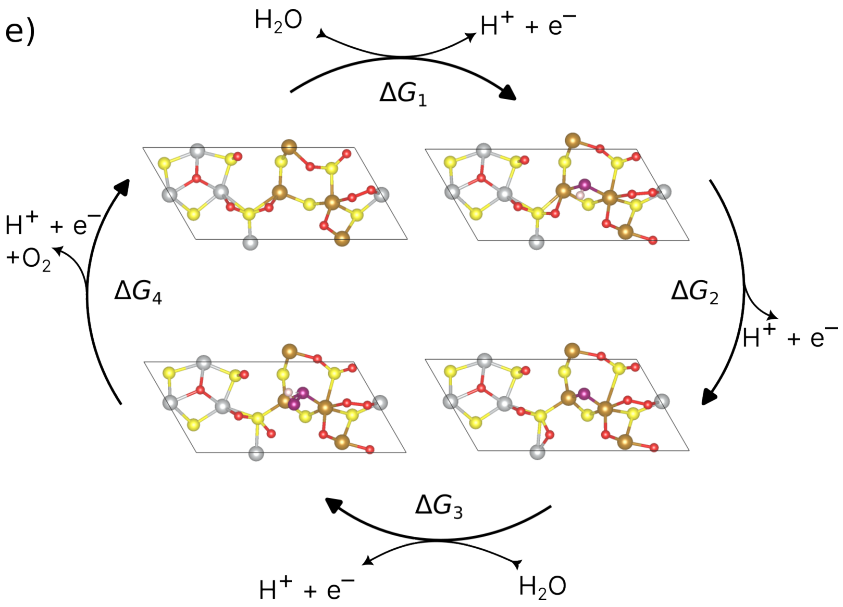
H2O
H+ + e−
ΔG1
H+ + e−
+O2
ΔG4
ΔG2
H+ + e−
ΔG3
H+ + e−
H2O

f)

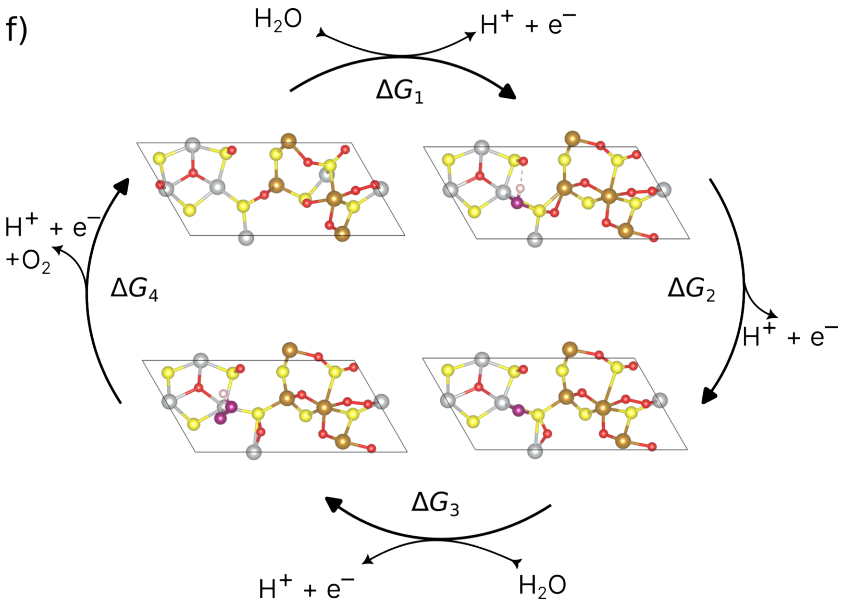
H2O
H+ + e−
ΔG1
H+ + e−
+O2
ΔG4
ΔG2
H+ + e−
ΔG3
H+ + e−
H2O

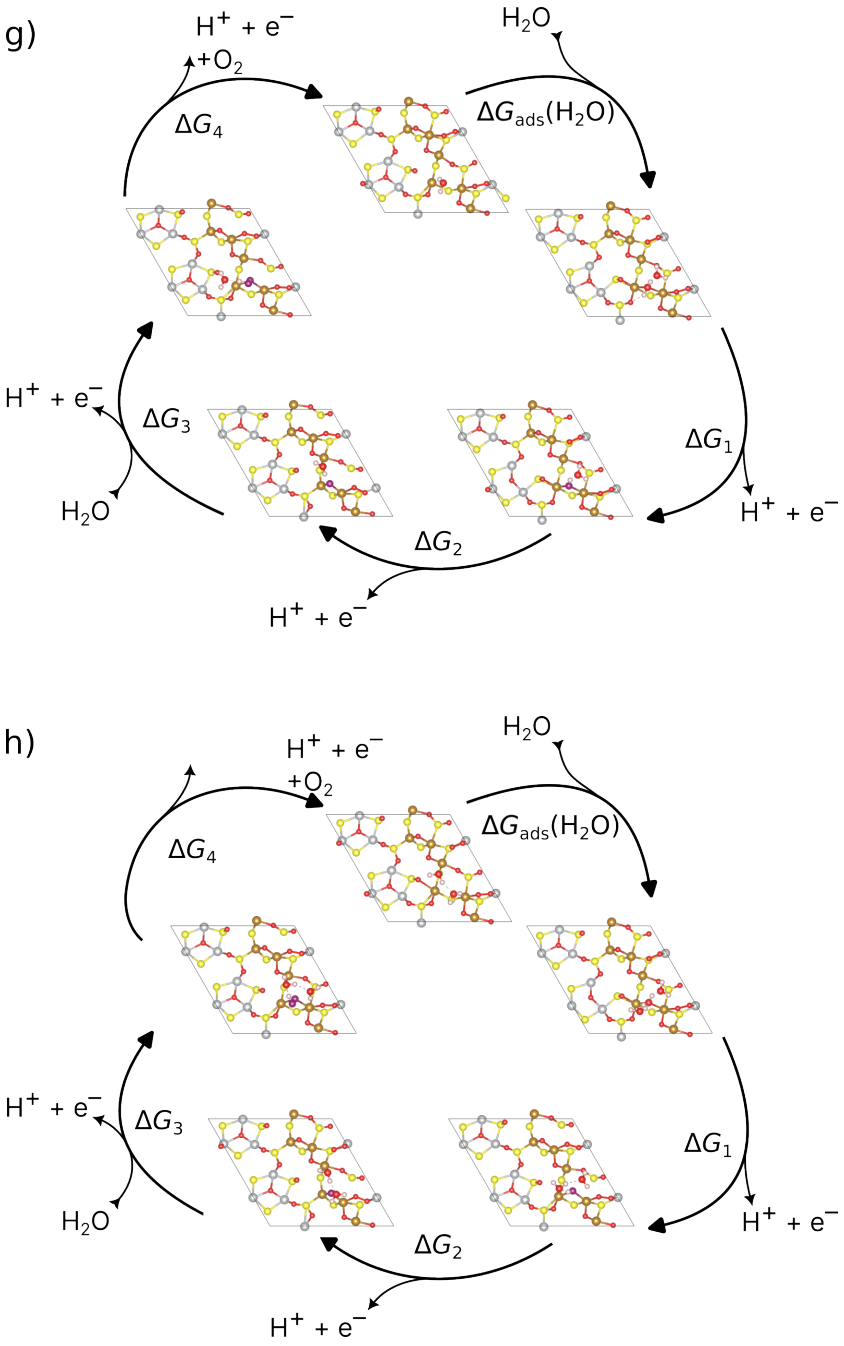

Figure S5. Visualization of the mononuclear OER pathway on various Pn surfaces, sites, and solvation treatments. a) pristine surface, Fe_{tet1} site; b) pristine surface, Ni_{tet2} site; c) 10*O coverage 1 × 1 surface cell, Fe_{tet1} site; d) 10*O coverage 1 × 1 surface cell, Ni_{tet2} site; e) 20*O coverage 2 × 1 surface cell, Fe_{tet1} site, VASPsol is either on or off (cf. case i) in **Table S5**); f) 20*O coverage 2 × 1 surface cell, Ni_{tet2} site; g) 20*O coverage 2 × 1 surface cell, Fe_{tet1} site, one explicit water molecule; h) 20*O coverage 2 × 1 surface cell, Fe_{tet1} site, two explicit water molecules.

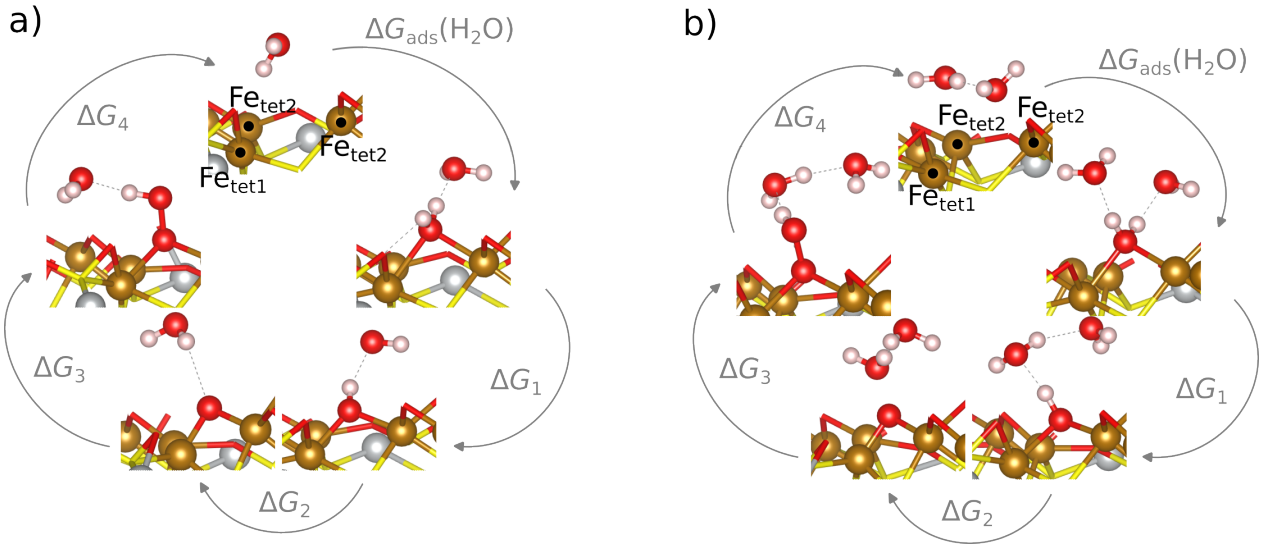

Figure S6. Visualization of the orientation of one (left) and two (right) explicit water molecules with Fe_{tet1} as the active site.

References

(1) Kresse, G.; Furthmüller, J. Efficient Iterative Schemes for Ab Initio Total-Energy Calculations Using a Plane-Wave Basis Set. *Physical Review B* **1996**, *54* (16), 11169–11186. https://doi.org/10.1103/PhysRevB.54.11169.

(2) Hammer, B.; Hansen, L. B.; Nørskov, J. K. Improved Adsorption Energetics within Density-Functional Theory Using Revised Perdew-Burke-Ernzerhof Functionals. *Phys. Rev. B* **1999**, *59* (11), 7413–7421. https://doi.org/10.1103/PhysRevB.59.7413.

(3) Kresse, G.; Hafner, J. Norm-Conserving and Ultrasoft Pseudopotentials for First-Row and Transition Elements. *Journal of Physics: Condensed Matter* **1994**, *6* (40), 8245–8257. https://doi.org/10.1088/0953-8984/6/40/015.

(4) Kresse, G.; Joubert, D. From Ultrasoft Pseudopotentials to the Projector Augmented-Wave Method. *Physical Review B* **1999**, *59* (3), 1758–1775. https://doi.org/10.1103/PhysRevB.59.1758.

(5) Grimme, S.; Ehrlich, S.; Goerigk, L. Effect of the Damping Function in Dispersion Corrected Density Functional Theory. *J Comput Chem* **2011**, *32* (7), 1456–1465. https://doi.org/10.1002/jcc.21759.

(6) Nørskov, J. K.; Rossmeisl, J.; Logadottir, A.; Lindqvist, L.; Kitchin, J. R.; Bligaard, T.; Jónsson, H. Origin of the Overpotential for Oxygen Reduction at a Fuel-Cell Cathode. *Journal of Physical Chemistry B* **2004**, *108* (46), 17886–17892. https://doi.org/10.1021/jp047349j.

(7) Sargeant, E.; Illas, F.; Rodríguez, P.; Calle-Vallejo, F. Importance of the Gas-Phase Error Correction for O2 When Using DFT to Model the Oxygen Reduction and Evolution Reactions. *Journal of Electroanalytical Chemistry* **2021**, *896*, 115178. https://doi.org/10.1016/j.jelechem.2021.115178.

(8) Exner, K. S. A Universal Descriptor for the Screening of Electrode Materials for Multiple-Electron Processes: Beyond the Thermodynamic Overpotential. *ACS Catalysis* **2020**, *10* (21), 12607–12617. https://doi.org/10.1021/acscatal.0c03865.

(9) Razzaq, S.; Exner, K. S. Materials Screening by the Descriptor $G_{max}(\eta)$: The Free-Energy Span Model in Electrocatalysis. *ACS Catal.* **2023**, *13* (3), 1740–1758. https://doi.org/10.1021/acscatal.2c03997.